In vivo photothermal therapy monitored by multi-position calibrated photoacoustic thermometer

Kuan Peng [a], Yongjun Wang [a], Lingfeng Li [a], Jiaxi Zhang [a], Haobin Chen [a], Jiaying Xiao [a,b,c,*]

[a] Department of Biomedical Engineering, School of Basic Medical Science, Central South University, Changsha 410083, China
[b] Shenzhen Research Institute, Central South University, Shenzhen 518057, China
[c] State Key Laboratory of Low-Dimensional Quantum Physics, Department of Physics, Tsinghua University, Beijing 100084, China

ARTICLE INFO

ABSTRACT

With the ability of monitoring both temperature and photothermal agents, the photoacoustic (PA) imaging is a promising guiding tool for the photothermal therapy (PTT). The calibration line which depicts the relative variation of PA amplitude with the temperature should be obtained before using PA thermometer. In existing study, a calibration line was generated based on the data from one spatial position, and used in the whole region of interesting (ROI). However, the generalization of this calibration line in ROI was not verified, especially for ROI with heterogeneous tissues. Moreover, the relationship between the distributions of photothermal agents and effective treatment area is not clear, hindering using photothermal agents' distribution to optimize the administration-therapy interval. In this study, the distribution of effective photothermal agents and temperature in subcutaneously transplanted tumor mouse models were continuously monitored by 3D photoacoustic/ ultrasonic dual-modality imaging in 8 h after administration. With multiple micro-temperature probes in tumor and surrounding normal tissue, the PA thermometer was calibrated and evaluated at multiple spatial positions for the first time. The generalization in homologous tissue and tissue specificity in heterogeneous tissues of the PA thermometer calibration line were verified. Our study not only validated the effectivity of PA thermometer by proving the generalization of calibration line, but also removes a major obstacle that prevents applying the PA thermometer to a heterogeneous tissues ROI. The positive correlation between the proportion of effective treatment area and the proportion of effective photothermal agent area in the tumor was observed. Since the latter can be monitored with fast PA imaging, PA imaging can be employed as a convenient tool for seeking optimal administration-treatment interval.

1. Introduction

By using exogenous photothermal agents with high optical-thermal conversion efficiency, tumor-targeting ability, and near-infrared absorption spectrum, photothermal therapy can selectively heat the cancerous lesion to cause tumor necrosis while sparing surrounding healthy tissue [1]. Compared with tumor ablation techniques widely used in clinical practice, the PTT with an exogenous photothermal agent has some appealing advantages, such as non-invasiveness, high tumor specificity, and spatial-temporal controllability [2]. Temperature and treatment duration are two key parameters that determine the effectiveness of PTT [3]. By measuring the temperature field during PTT and merging it with the structure imaging, the treatment area in the tissue can be estimated and adjusted [4]. The most widely used technologies at

present for temperature monitoring in PTT are invasive temperature sensors [5–7], magnetic resonance thermal imaging (MRTI) [8,9], and thermal cameras [10,11]. The invasive temperature sensors are inserted into the tumor to provide some spatially sparse samples of the temperature field, but they cannot be used to map the temperature distribution of the entire treatment area. Besides its high cost, MRTI is inconvenient to perform PTT in the barrel of MRI, and an antimagnetic equipment is required. A thermal camera only gives a surface projection of the temperature field thus failing to provide a low boundary of the treatment region. Ultrasound (US)-based thermometry is also a non-invasive temperature monitoring method that has been investigated for decades [12–14]. This method employs the time delay of the echoes to assess temperature-dependent changes in the speed of sound. However, since the size of the treatment region is usually far smaller than that of

the imaging area, this temperature-induced variation of echo time delay is quite small, and its detection could be disturbed by respiratory movement when it is applied in vivo [15]. This defect limits the ability of ultrasound thermometry to detect a small variation in temperature.

Photoacoustic imaging is a hybrid imaging modality that employs ultrasound to detect optical contrast [16]. The image reconstructed from the PA signal depicts the distribution of optical absorbers in biological tissue [17–19]. The intensity of the PA source is proportional to the Grüneisen parameter, which is sensitive to changes in temperature [20]. As a result, the photoacoustic thermometry can be built by analyzing the amplitude variation of the PA source before and after heating. Moreover, the distribution of the exogenous photothermal agents in biological tissue is also important information that has a great influence on photothermal efficacy [21]. The therapeutic temperature field can only be produced when the photothermal agent is properly located in lesions. Given the high photothermal conversion efficiency, the photothermal agent is also a high-performance contrast agent for photoacoustic imaging [22]. With the ability to obtain the photothermal agent distribution and monitor the photothermal temperature, PA imaging is a desirable guiding tool for photothermal therapy. Great efforts have been devoted to developing this technology. PA imaging was employed to monitor the distribution of endogenous photothermal agents and temperature field in photothermal therapy [23–25]. A thermal-energy-memory-based photoacoustic thermometry was proposed to remove the requirement for tissue's reference temperature [26]. The output of PA thermometer was used as the feed-back controller for photothermal therapy [27]. An integrated photoacoustic guided system was developed for endovenous laser ablation [28].

Although great progress has been made in recent years, PA monitored photothermal therapy still need to be further investigated. The calibration line which depicts the relative variation of PA amplitude with the temperature should be obtained before using PA thermometer. In existing study, a calibration line was generated based on the data from one spatial position, and used in the whole region of interesting. However, the generalization of this calibration line in ROI was not verified, especially for ROI with heterogeneous tissues. Moreover, the relationship between the distributions of photothermal agents and effective treatment area is not clear, hindering using photothermal agents' distribution to optimize the administration-therapy interval. In this work, the distribution of effective photothermal agents and temperature in subcutaneously transplanted tumor mouse models were continuously monitored by 3D photoacoustic/ ultrasonic dual-modality imaging in 8 h after administration. With multiple micro-temperature probes in tumor and surrounding normal tissue, the PA thermometer was calibrated and evaluated at multiple spatial positions. The generalization of

the PA thermometer calibration line in a heterogeneous tissues ROI and in different experiment subjects was investigated. The relationship between the proportion of effective treatment area and the proportion of effective photothermal agent area in the tumor was also explored.

2. Method

2.1. System setup and data acquisition

The diagram of the system is shown in Fig. 1. The dual-model imaging system was assembled with the photothermal therapy system. The ultrasound images and photoacoustic images were acquired before and during the photothermal therapy to monitor the therapy process. Both ultrasound and photoacoustic signals were collected by a line-array transducer of 128 elements (L11–5 V, Verasonics, USA). Its aperture, pitch, elevation focus, central frequency and bandwidth is 38 mm, 0.3 mm, 18 mm, 7.5 MHz and 80%, respectively. The signal was recorded by a multi-channel ultrasound acquisition system (Vantage 256, Verasonics, USA). An optical parametric oscillator (OPO) tunable laser (SpitLight 600, Innolas, Germany) was employed as the radiation source for photoacoustic imaging. It produced 5 ns pulses with a repetition rate of 20 Hz. The energy of the laser pulse is 70 mJ at the wavelength of 950 nm. The photothermal therapy was carried out by a CW diode laser (LWIRL950, Laserwave, China). It generates 950 nm CW laser with a power of 2 W. The light from both lasers is combined by an optical combiner (BSW30, Thorlabs, USA), and then coupled into a 1 mm core diameter multimode optical fiber (FT1000EMT, Thorlabs, USA) by an optical fiber coupler (MBT610D/M, Thorlabs, USA). The energy density of the pulse laser and power density of the CW laser on the surface of the tumor was measured as 28 mJ/cm^2 and 0.6 W/cm^2, respectively. These values satisfy the American National Standard Institute (ANSI) limit for human skin exposure [29]. A thermocouple thermometer (TA612C, TASI, China), which has three 0.1 mm diameter probes, was used to calibrate the PA thermometer.

When starting the PA data acquisition, the Vantage 256 sent out a synchronization signal to trigger a 950 nm laser pulse from the OPO. Since the amplitude of the PA source is quite sensitive to the irradiation fluence, the energies of the laser pulses were monitored by a photodiode detector (SM05PD1A, Thorlabs, USA). The pixel values of the PA image were normalized to the corresponding pulse energy to compensate the laser energy fluctuation. The PA data was also used to evaluate the distribution of both temperature and photothermal agents. The US imaging was taken 50 μs after each PA requisition. The US pulse-echo sequence was initiated at the beginning of data acquisition when a laser pulse is generated. The ultrasonic pulse transmission was delayed
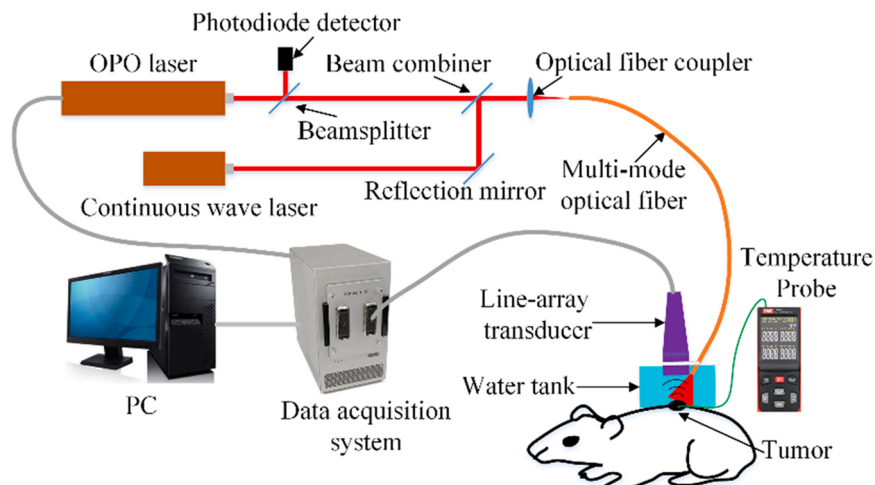

Fig. 1. System setup.

by $50\mu s$ to separate the PA signal and US signal in time domain. A total 4096 RF data points were acquired with a sampling frequency of $31.25MHz$. The first 1563 data points were used by PA imaging and the rest were used by US imaging. Since $50\mu s$ is far short than the respiratory cycle, the two images can be easily registered. The successive PA image and US image are composed of one imaging frame. Both US and PA data were reconstructed with delay and sum beamforming methods to generate the images [30].

A water tank, whose bottom was sealed by a thin polyethylene film, was used to provide acoustic coupling between experiment subject and transducer. The water temperature was held at a constant of 35 ^oC with an electronically thermo-controller (e50, EHEIM, Germany) to avoid hypothermia in mice.

2.2. Photoacoustic thermometry

With the irradiation of a nanosecond laser pulse, the optical absorber is heated and then thermal expanded because of photothermal conversion. The subsequent photoacoustic wave can be expressed as [31]:

$$p_{PA} = \Gamma\eta\mu_a\phi\delta t \qquad (1)$$

Where p_{PA} is the amplitude of PA source, Γ is the Grüneisen parameter, η is the conversion efficiency of non-radiative relaxation, μ_a is the optical absorption coefficient, ϕ is the optical intensity, δt is the laser pulse width. During the period of a photothermal therapy process, η, μ_a, ϕ and δt are assumed to be invariant. As a result, p_{PA} is mainly dependent on Γ. Γ is determined by the following equation [32]:

$$\Gamma = \beta c_s^2 / C_p \qquad (2)$$

Where β is the thermal coefficient of volume expression, c_s is the speed of sound, and C_p is the heat capacity of constant pressure. It has been proved that both of β and c_s are temperature dependent [33]. Therefore, Γ is also temperature dependent. Some studies demonstrated that Γ is linear dependent on the temperature in the range of 10–55 ^oC for water-based and fatty-based tissue [20]. As a result, Γ can be determined approximately by temperature as:

$$\Gamma = a + bT \qquad (3)$$

Where a and b are tissue dependent constant. T is temperature. Substituting Eq. (3) into Eq. (1), we can get the following equation:

$$p_{PA}(T) = (a + bT)\eta\mu_a\phi\delta t \qquad (4)$$

The temperature before and during the thermal therapy are indicated by T_0 and T_1. If the amplitude of PA source before and during thermal therapy are measured to be $p_{PA}^{ref}(T_0)$ and $p_{PA}(T_1)$, the temperature T_1 can be calculated as:

$$T_1 = c + dp_{PA}(T_1) / p_{PA}^{ref}(T_0) \quad with \ \ c = -a/b, \ \ d = (T_0 - c) \qquad (5)$$

c is a tissue-dependent constant, d is determined by both reference temperature T_0 and c. They can be obtained by the system calibration procedure.

To imply the photoacoustic thermometry, a reference frame of US/PA imaging has to be acquired at the reference temperature T_0. Then, the variation of PA source amplitudes at each imaging position was calculated based on the reference image and heating image. As a result, the imaging displacement caused by respiratory movement and sound speed variation has to be compensated for the heating image. To separate these two kinds of imaging displacement, a respiratory movement evaluation area (RMEA), which is far away from the treatment area (TA) and keeps a constant temperature during the treatment, was used to evaluate respiratory movement. For temperature measurement, PA/US images were collected at the speed of 20 $frames/s$. Since US imaging provides the structure information of tissue, it is suitable for respiratory movement evaluation. The time interval between the PA and US images in the

same frame is far shorter than a respiratory cycle, these two images can be considered to be collected in the same respiratory state. Therefore, the respiratory movement was compensated based on US images in this study. The imaging displacement caused by the respiratory movement was evaluated by a 2-D speckle tracking algorithm (STA) [34]. It calculates the image structural similarity in RMEA between the US images of heating frame and reference frame. The temperature calculation frame (TCF) was determined by the smallest mean value of the auto-correlation coefficient (ACC) in RMEA concerning the reference frame [34]. Since the imaging displacement caused by temperature-variated sound speed is far smaller than that caused by respiratory movement [35], using 2-D STA can align the pixels in TA of TCF to the reference image to compensate for the imaging displacement caused by temperature-variated sound speed. After compensating for the imaging displaces, the ratio between the PA amplitude of heating image and reference image can be obtained. The temperature field can be calculated by using Eq. (5).

The thermal couple probes were inserted into the heating region to do the system calibration. The inserting procedure was guided by US imaging. After acquiring the reference frame, the treatment area was irradiated by CW laser for 5 min. During this procedure, PA/US images were collected at the speed of 20 $frames/s$. The TCFs were chosen by using the method described previously. The temperature readings corresponding to these TCFs were recorded by the thermal couple temperature probes. A linear fitting based on these data can give the estimation of c and d in Eq. (5).

2.3. P-dots synthesis

The band gap of conjugated polymers can be effectively tuned by a design approach through donor-acceptor interactions [36], we choose benzodithiophene (BDT) as a donor due to its excellent electron donating ability and triazoloquinoxaline (TaQX) as the acceptor due to the exclusively electron-deficient backbones. Polymer (benzo[1,2-b:4, 5-b']dithiophene,4,8-bis[5-(2-ethylhexyl)− 2-thienyl]− 2, 6-diyl)-co-([1−3]triazolo[3,4-g]quinoxaline,6,7-bis[3-tri-fluoromethyl-4-[(2-ethylhexyl)oxy] phenyl]− 4,9-diyl) (PBDT-TaQX, Fig. 2a) P-dots were prepared by nanoprecipitation method [37,38]. The conjugated polymers PBDT-TaQX were chosen as the basic component, mixed with amphiphilic polymer poly (styrene-co-maleic anhydride) (PSMA) in tetrahydrofuran (THF), and the mixed solution was rapidly injected into pure water under vigorous sonication. THF was removed by bubbling N_2 through the solution on a hot plate, then filtered through an aqueous phase 0.22 μm filter. The average hydrodynamic diameter of P-dots is about 21 nm (Fig. 2b). The optical properties of P-dots were examined by using the absorption spectrometer. P-dots showed strong near-infrared absorption with a peak at 947 nm (Fig. 2c).

2.4. Xenograft tumor mouse model

Colorectal cancer cells (HCT-116) and 8-week-old immunodeficient nude mice (BALB/c-Nude, GemPharmatech) were used to establish a xenograft tumor mouse model. 100 μL suspension cell fluid, whose concentration is 10^7 cell/mL, was subcutaneously injected into the back of mice to initiate the tumor growth. The mouse model was ready for the experiment when the diameter of the tumor grew to about 10mm. During the experiment, the mice is anesthetized with a combination of isoflurane (0.5–2.0%) and oxygen (0.5 L/min). The P-dots solution was administrated trans-dermally. After the experimental procedures, the mice were euthanized by carbon dioxide asphyxiation. All procedures were performed following an animal protocol approved by the Institutional Animal Care and Use Committee at The Central South University.
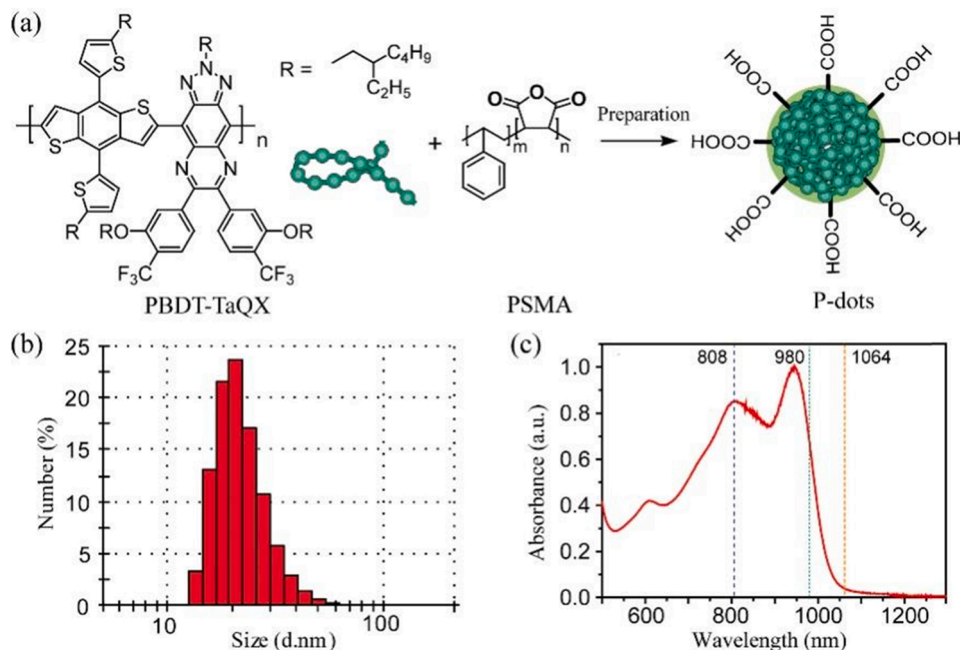
Fig. 2. (a) P-dots were prepared from PBDT-TaQX and the amphiphilic polymer PSMA by nanoprecipitation; (b) Hydrodynamic sizes measured by dynamic light scattering of the P-dots dispersed in water; (c) Absorption spectra of P-dots.

3. Results

3.1. System calibration of photoacoustic thermometer

To calibrate and evaluate the photoacoustic thermometer, a mouse was anesthetized. Then, three acicular thermal-couple temperature probes were inserted into the ROI and fixed with adhesive tape. Two probes are in tumor, and the third probe is in normal tissue. 85 μL P-dots solution, whose concentration is 150 $\mu g/mL$, was injected locally into the tumor. Before heating with CW laser, a frame of US/PA image was acquired to provide the reference data. The US image, which is shown in Fig. 3a, was used to determine the positions of the tumor and temperature probes. The tumor (low echo area, indicated by a yellow circle) and temperature probes (high echo area, indicated by red and blue circles) can be discriminated in it. The RMEA is indicated by a green box. This image is the reference for the imaging displacement compensation. The initiate temperature T_0 was given by the temperature probes as 35 ^oC. After the P-dots injection, the tumor is heated by 5 min of CW laser illumination immediately. The readings of three temperature probes during this heating process are given in Fig. 3b. It indicates that the probe readings were stable after 4 min of CW laser illumination. Therefore, 5 min of CW laser illumination is long enough to create a stable temperature field in our experiment. The US/ PA images were

collected at a repetition frequency of 20 $frames/s$ for each measurement. Each measurement takes 1 s, and the time interval between two succeeding measurements is 10 s. According to our test, the pulsed laser introduced temperature increase is less than 0.1 ^oC during each measurement, so it can be ignored. After compensating for the imaging displacement, the average PA amplitude in the temperature probe area (p_{PA}^{TCF}) was calculated for the PA image in each TCF. These values were further divided with their correspondences from the reference frame (p_{PA}^{ref}) to evaluate the heating-induced PA amplitude variation. The readings of the temperature probes, which are corresponding to the TCF collection time points, were also recorded. These calibration data were presented in Fig. 4a and Fig. 4b, in which the linear relationship between these two parameters can be observed. The linear fitting results were also shown in Fig. 4a and Fig. 4b. Since the temperature increasement of three probes were different from each other, only part of the calibration data from probe 1 and probe 2 was present in Fig. 4a, but the linear fitting results and the errors were calculated based on all of the calibration data. With these data, the temperature resolution of our system can be calculated as 0.18 ^oC based on the average standard deviation of the PA signal amplitude of 0.5% [15]. It can be found that the two calibration lines (indicated by red line and black line) in the tumor are quite close with each other. To evaluate the accuracy quantitatively, the PA thermometer results were compared with the temperature probe
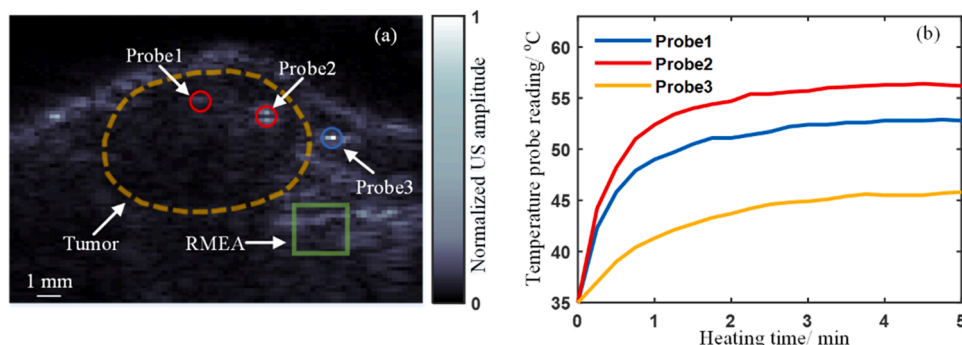

Fig. 3. (a)The US image of the reference frame. RMEA indicates respiratory movement evaluation area; (b) The probe reading during the heating procedure.
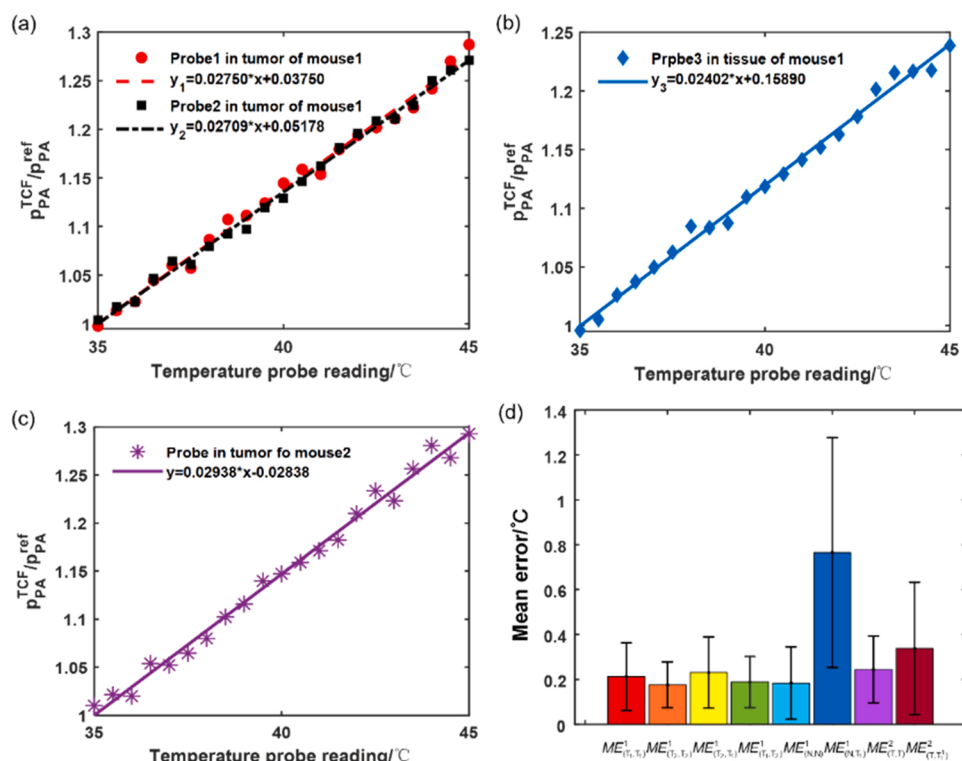
Fig. 4. (a) The calibration data and fitting lines of two probes in tumor of mouse 1; (b) The calibration data and fitting line of the probe in normal tissue of mouse 1; (c) The calibration data and fitting line of the probe in tumor of mouse 2; (d) The mean errors (MEs) of measurement results obtained by PA thermometer in calibration experiment. The superscript of ME represents the index of mouse. T_1 and T_2 in subscription of ME represent the probe 1 and probe 2 in tumor areas, N in subscription of ME represent the probe in normal tissue area; The first label in subscription of ME indicates where the calibration data comes from; The second label in subscription of ME indicates where the used calibration line comes from; Specially, T_1^1 means the calibration line generated by the probe 1 of mouse 1.

readings, the results are presented in Fig. 4d. The accuracy of the PA thermometer was evaluated at each calibration position in tumor using its own corresponding calibration line, the mean errors (MEs) were calculated as 0.21 ^oC and 0.18^oC, respectively, as shown the first two bars in Fig. 4d. When these two calibration lines were applied to other calibration positions in tumor, the MEs only slightly increased to 0.23 ^oC and 0.19^oC, as shown the third and fourth bars in Fig. 4d. The performance of the calibration lines, which are generated from different spatial positions in the same kind of tissue, are quite close to each other. The error didn't increase significantly when the calibration line is applied to a location other than its own calibration position in this case. However, this conclusion doesn't hold for different kinds of tissues. Although PA thermometer obtained an acceptable accuracy by using its own calibration line in normal tissue (as shown the fifth bar in Fig. 4d), significant distinction was observed between the calibration lines which are corresponding to tumor and normal tissue, as indicated in Fig. 4b. Noticeable aberration will be induced by using an inaccurate calibration line in PA thermometer, as shown the sixth bar in Fig. 4d. In our experiment, the ME and max error are as large as 0.77 and 1.3^oC if the tumor calibration line is employed to generate the temperature of normal tissue. The temperature distribution in a heterogeneous tissues

ROI were present in Fig. 5. Since the optimal temperature range of PTT starts from 43 ^oC[39], the area whose temperature is higher than 43 ^oC is defined as effective treatment area in this work. Only the temperature distribution of effective treatment area was present in the temperature measuring result. The temperature increasement in normal tissue was caused by the photothermal agents infiltrated from the tumor. The temperatures of tumor and tissue in Fig. 5b were generated with their own calibration line, while only the calibration line of tumor was applied in Fig. 5a. It's obviously that the inaccurate calibration line underestimated the temperature of normal tissue (nearly 2 ^oC). Unnecessary thermal damage to the normal tissue could be caused if this unfaithful temperature distribution is used by the feedback control of effective treatment area in PTT.

In addition, we also investigated the generalization of PA thermometer calibration line in normal tissue. Since the ROI of the previous experiment didn't have enough space for the fourth temperature probe, this study was carried out in a new ROI. Two thermocouple probes were inserted into the normal tissue in order to generate the calibration lines for PA thermometer, as shown in Fig. 6a. The calibration result is shown in Fig. 6b. The accuracy of the PA thermometer was evaluated at each calibration position in normal tissue using its own corresponding
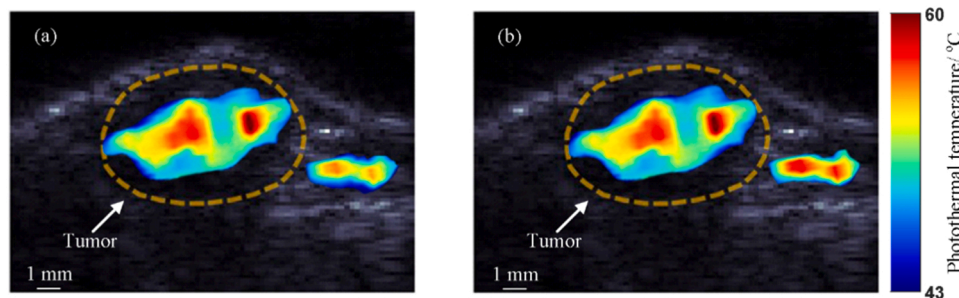

Fig. 5. (a) The temperature distribution in a heterogeneous tissues ROI generated with the calibration line of tumor; (b) The temperatures of tumor and tissue generated with their own calibration line.
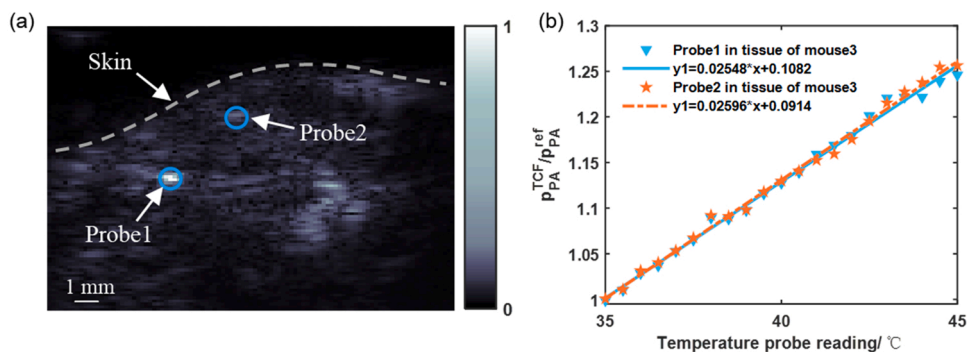
Fig. 6. (a) The position of two temperature probes in normal tissue; (b) The calibration data and fitting lines of two probes in normal tissue.

calibration line. The MEs were calculated as 0.23^oC and 0.20^oC, respectively. When these two calibration lines were applied to other calibration positions in normal tissue, the MEs slightly increased to 0.25^oC and 0.24^oC. These results confirmed that the PA thermometer calibration line also can be generalized in normal tissue.

The individual difference of the calibration line for the PA thermometer was also investigated. Another xenograft tumor mouse model was built according to the procedure described in the Method section. A micro-probe was insert into the tumor area to generate the calibration line. The result is shown in Fig. 4c. The ME of the PA thermometer was calculated as 0.24 ^oC if the calibration line of its own was used. This measurement accuracy was comparable to the first experiment. However, if the tumor calibration line from the previous experiment was implied, the ME was significantly increased to 0.34^oC. It's obvious that the calibration line has an individual difference, so it has to be updated for each experiment subject.

3.2. Photothermal therapy monitoring based on PA/US imaging

Both of the PA amplitude and photothermal energy generation are dependent on the local optical fluence and photothermal agent concentration. The CW laser and pulsed laser, which share the same wavelength and emit from the same optical fiber, were employed in this work. As a result, the distribution of the PA amplitude can be used to assess the distribution of the effective photothermal agent in PTT. To observe the variation of the photothermal temperature field with the dynamically changed distribution of effective photothermal agent, the tumor with locally injected P-dots was repeatedly heated and scanned with PA/US imaging for different administration-therapy intervals. The

experiment was carried out with the first experiment subject in the previous section. The distribution of the effective photothermal agent and temperature field were collected simultaneously at 0, 2, 4, 6, and 8 h after the injection. Since the amplitude of the PA source was sensitive to the temperature, a reference frame was generated before the heating in each monitor. To compensate for the imaging displacement caused by respiratory movement between different monitor time, the reference frames at 2, 4, 6, and 8 h monitors were chosen from an acquisition serial that contains 20 frames of PA/US images. These frames were acquired in one second at the corresponding monitor time. The frame, which has the smallest US imaging displacement relative to the reference frame at 0 h, was chosen as the reference frame at the corresponding monitor time. For the effective photothermal agent distribution changes dynamically, and 5 min CW laser irradiation was needed to stabilize the photothermal temperature field, the variation of effective photothermal agent distribution during 5 min was studied first. At 0 h and 8 h after the injection, two effective photothermal agent distributions were collected through PA imaging with 5 min intervals, as shown in Fig. 7. The similarity of these two images was evaluated by Pearson correlation coefficient (PCC) [40] and structure similarity index measure (SSIM) [41]. The results are shown in Table 1. It can be found

Table 1
The similarity between two P-dots distributions collected with 5 min interval.

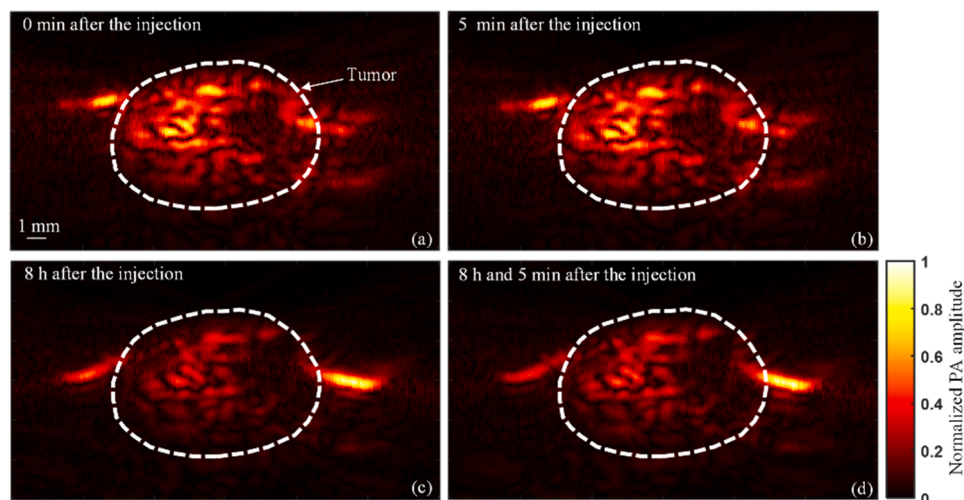| Monitor time	Pearson correlation coefficient	structure similarity index measure
0 h	0.96	0.98
8 h	0.98	0.99

Fig. 7. The variation of P-dots distribution within 5 min at 0 h and 8 h after the injection.

that the variation of effective photothermal agent distribution during 5 min is quite small, so it is negligible. The PA images in each reference frame provide the effective photothermal agent distributions at different monitor time points, as shown in Fig. 8. The diffusion process of the effective photothermal agent in the tumor can be clearly observed. Within 6 h after the injection, the distribution area of the effective photothermal agent becomes larger in the tumor with an increased administration-treatment time, as shown in Fig. 8a-Fig. 8d. But 8 h after the injection, the content of effective photothermal agent in the tumor decreased because of the metabolism. The max concentration of the effective photothermal agent, which is evaluated by the max PA amplitude, decreased steadily. It reduced by 27% within 8 h after the injection, as shown in Fig. 8 f. After 5 min CW laser irradiation, the stable effective photothermal temperature field corresponding to different monitor times were established and measured with a PA thermometer, as shown in Fig. 9a-Fig. 9e. With the decrease of the effective photothermal agent concentration, the highest temperature that the treatment can reach also drop from 64 ^{o}C to 51 ^{o}C during the time of monitor, as shown in Fig. 9 f. The area of the effective treatment region increased with the diffusion of the effective photothermal agent in the tumor. As shown in Fig. 9 g, the peak value reached at 6 h after the injection. Then, the effective treatment region shrank at 8 h after the injection when the photothermal agent began to be discharged from the tumor. To further confirm the observation of the 2D results, the 3D distributions of the effective photothermal agent and effective temperature field were measured after the injection. 80 2D slices were collected with a spatial interval of 0.05 mm to generate the 3D result. To obtain 1 slice, 20 frames of PA/US images should be acquired before and after the heating to produce the reference frame and TCF. The final 3D images were generated by a 3D visual software (Amira, USA). The 3D distributions of the effective photothermal agent at 0 h and 6 h were given in Fig. 10a and Fig. 10c. The 3D distributions of the effective temperature field at 0 h and 6 h were given in Fig. 10b and Fig. 10d. Comparing with the monitor result right after the injection, the sizes of both the effective photothermal agent area and effective temperature field with 6 h administration-treatment interval increased significantly in both depth and lateral directions. To quantitatively describe the distribution of the effective photothermal agent and effective photothermal temperature field in the tumor, the percentage of effective photothermal agent voxels and effective treatment area voxels inside the tumor boundary were calculated for the different times after injection. The results were presented in Table 2. The tumor voxels were identified by the abnormal low-echo value in the co-registered 3D US images. The position, whose PA amplitude is larger than 3 times of background, is considered to have effective photothermal agent in this study. It can be observed that the percentage of effective photothermal agent distribution area in the tumor reached its maximum at about 6 h after the injection. This administration-treatment time interval was coincident with the time when the largest effective treatment area can be reached. Moreover, the positive correlation between the proportion of effective treatment area and the proportion of photothermal agent area in the tumor can be clearly observed in Table 2. These results suggest that the optimal administration-treatment interval can be determined by monitoring the distribution of the effective photothermal agent in the tumor. Since the PA/US imaging, which is employed to determine the effective photothermal agent distribution, can be carried out quite fast. This method is more convenient than the heating and temperature measuring procedure.

4. Discussion and conclusion

Although the use of the PA thermometer for photothermal therapy guidance has been intensely studied for more than ten years, the calibration and evaluation of the PA thermometer were usually based on the data from only one calibration position, especially for those researches carried out in vivo. The generalization of the calibration line in the whole ROI has not been investigated yet. To address this issue, Multiple micro-temperature probes, which were deployed at different positions in the tumor and surround normal tissue, were employed to calibrate the PA thermometer in this study. Several calibration lines generated from the homologous tissue and heterologous tissue were compared. The result verified the generalization of the calibration line in homologous tissue. Appling a calibration line to the location other than the calibration position in the same kind of tissue doesn't noticeable increase the measurement error of PA thermometer. Therefore, one calibration position is accurate enough for the measurement in the same kind of tissue. Moreover, the treatment temperature didn't reach the boundary of the tumor in our experiment which is caused by the unsatisfied distribution of photothermal agent in tumor. It is the situation which could be avoided with the proposed monitoring technique. For a tumor of large-size, the photothermal agent should be injected into multiple positions of it to make sure treatment temperature reach the lesion boundary. However, this strategy also increases the risk of thermal damage to the surrounding normal tissue. As a result, a thermometer that can work
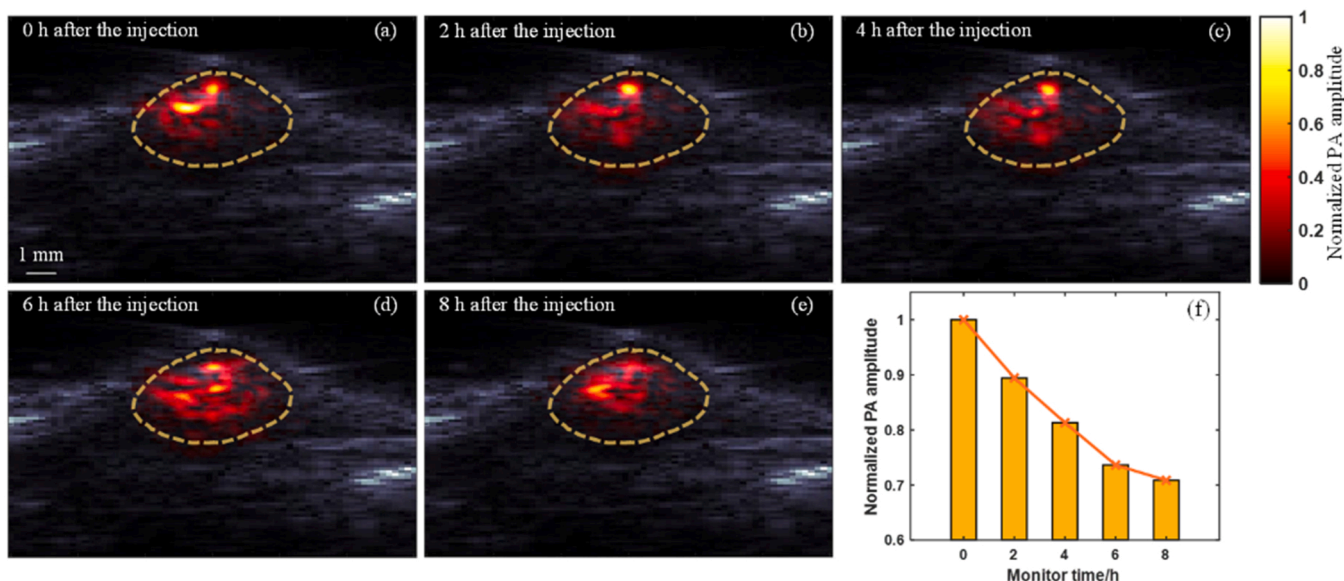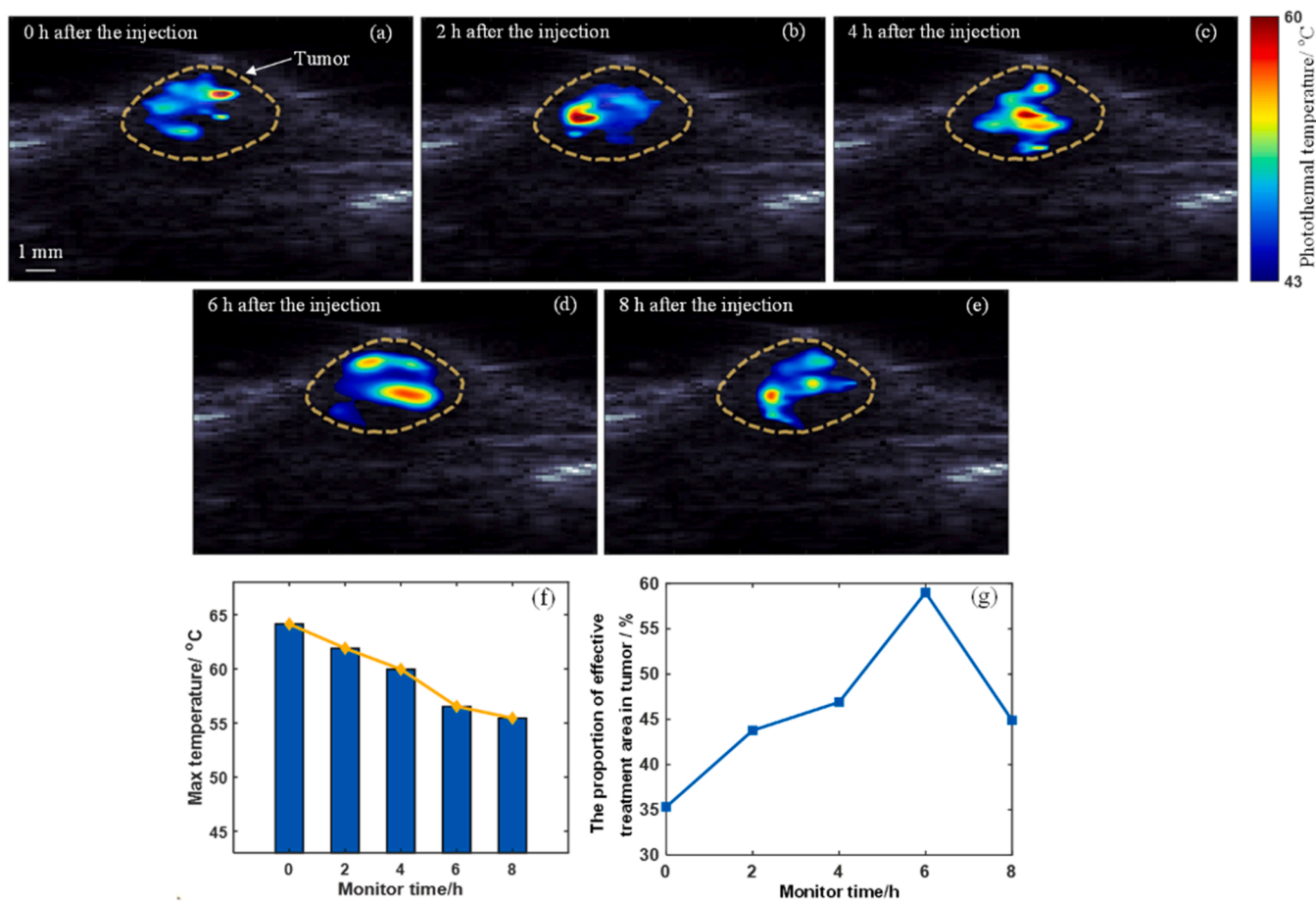

Fig. 8. (a)-(e) The diffusion of the effective photothermal agent in the tumor; (f) The change of max PA signal amplitude with the monitor time.

Fig. 9. (a)-(e) The effective photothermal temperature field in the tumor at different monitor time; (f) The max photothermal temperature at different monitor time; (g) The percentage change of the effective photothermal treatment area within the tumor.

reliably in both tumor and normal tissue is crucial for an accurate PTT. In our study, the tissue specificity of PA thermometer calibration line was observed for the first time. Our results indicate that the PA thermometer should be calibrated for each tissue if the ROI is composed of heterogeneous tissues. The discrimination of lesion and normal tissue can be carried out with structure imaging such as US or the combination of PA imaging and targeted photothermal agents. By deploying multiple micro-probes in proper positions, the calibration of PA thermometer in multiple tissues can still be executed in a single calibration procedure. Calibrating the PA thermometer properly is quite important for the estimation of effective therapeutic area, which is determined by the measurement of temperature. In our experiment, Appling the calibration line of tumor to the surrounding area in PA thermometer could cause a measurement error as high as 2^oC, and worse the feedback control performance which is employed to regulate the effective therapeutic area. Moreover, a significant individual difference was observed for the PA thermometer calibration line in our experiments. Even requiring the data by using the same equipment with the same procedure from the same kind of xenograft tumor mouse model, using the calibration line from another experiment subject may cause an abnormal increase of measurement error. It means that the relationship between the Grüneisen parameter and temperature may change noticeably for the same kind of tissue from different individuals. As a result, system calibration is necessary for each experiment subject when using the PA thermometer.

Although the usage of extraneous photothermal agent has many attractive advantages over the endogenous photothermal agent in PTT, the determination of administration-therapy interval is a troublesome problem. Although the distribution of extraneous photothermal agent could be monitored with PA imaging, the relationship between the

distributions of photothermal agent and temperature is still unclear, because the trade-off between high concentration and distribution range exists, especially for topical administration. The PA amplitude is not proportional to the actual photothermal agent concentration because of the disturbance of optical fluence. However, both of the PA amplitude and photothermal energy generation are dependent on the local photothermal agent concentration and optical fluence. By using the lasers with the same wavelength and identical emitted path for PA imaging and PTT, PA amplitude can be employed to assess the effective photothermal agent concentration that can function in PTT. In our experiment, the optimal distribution of effective treatment area in the tumor wasn't reached with high concentration but less diffusive distribution of effective photothermal agent. Although higher local temperature can be generated by high concentration of effective photothermal agent, the heat energy spread efficiency through heat conduction seems not be adequate enough in tumor. Moreover, this kind of distribution pattern of effective photothermal agent also doesn't fully utilize the irradiation energy, since a laser spot, which covers the whole lesion, is usually applied in PTT. In our experiment, the positive correlation between the proportion of effective treatment area and the proportion of effective photothermal agent occupied area in the tumor was observed, which indicates that the latter parameter can be employed to denote the most desirable temperature distribution. Since distribution of effective photothermal agent can be acquired with the fast PA imaging, it can be utilized to provide a convenient means to determine the administration-therapy interval in PTT.

There are still some issues in our study need to be further investigated. Firstly, the number of experiment subjects are still limited. More experiments should be carried out to strengthen the statistical
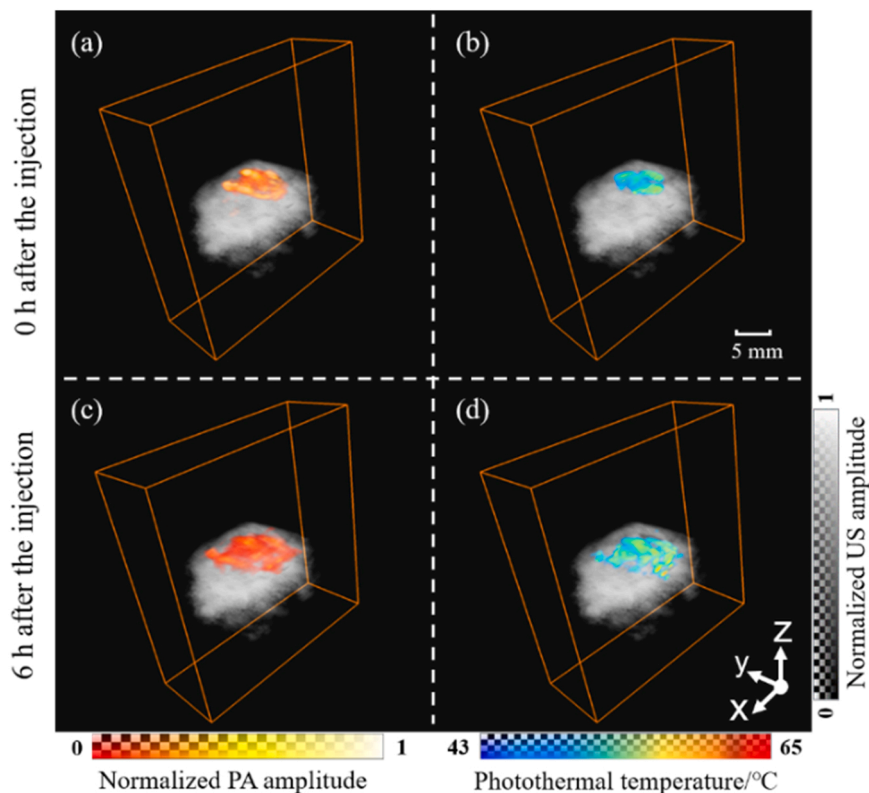
Fig. 10. (a-b) The 3D distribution of effective photothermal agent and effective temperature field in tumor at 0 h; (c-d) The 3D distribution of effective photothermal agent and temperature field in tumor at 6 h.

Table 2
The proportion of effective photothermal agent voxels and effective treatment area voxels in tumor region at different monitor time points.

Monitor time	0 h	2 h	4 h	6 h	8 h
The proportion of effective photothermal agent area in tumor	44.00%	56.75%	62.50%	80.06%	64.50%
The proportion of effective treatment area in tumor	28.93%	34.64%	45.30%	55.95%	46.72%

significance of our results. Secondly, the insert procedure of multiple individual probes is not quite convenient. The fiber Bragg grating (FBG) temperature sensor array [42], which bases on etching multiple micro-temperature probes on a small optical fiber, can be employed for the multi-position calibration in PA thermometer. Thirdly, only topical administration pattern of photothermal agents was investigated in this study. Considering the intravenous administration is also an important administration method used in PTT, the imaging guidance of the PTT based on intravenous administration will be explored in our future study with a biocompatibility and tumor targeting ability improved photothermal agent. Lastly, photothermal temperature in tissue is governed by the biological heat equation [43]. PA imaging can provide the tissue distribution of several key parameters in this equation such as photothermal source and blood perfusion rate. PA imaging may help to predict an accurate distribution of photothermal temperature in tissue.

In summary, the distribution of effective photothermal agents and temperature in subcutaneously transplanted tumor mouse models were continuously monitored by 3D photoacoustic/ ultrasonic dual-modality imaging in 8 h after administration in this study. With multiple micro-temperature probes in tumor and surrounding normal tissue, the PA thermometer was calibrated and evaluated at multiple spatial positions for the first time. The generalization in homologous tissue and tissue specificity in heterogeneous tissues of the PA thermometer calibration line were verified. The PA thermometer was applied in a ROI with heterogeneous tissues for the first time. The positive correlation between the proportion of effective treatment area and the proportion of effective photothermal agent occupied area in the tumor was found, which indicates that PA imaging can be employed as a convenient tool for seeking optimal administration-treatment interval.

Declaration of Competing Interest

The authors declare that they have no known competing financial interests or personal relationships that could have appeared to influence the work reported in this paper.

Data Availability

Data will be made available on request.

References

[1] D.F. Zhi, T. Yang, J. O'hagan, S.B. Zhang, R.F. Donnelly, Photothermal therapy, J. Control. Release 325 (2020) 52–71, https://doi.org/10.1016/j. jconrel.2020.06.032.

[2] S. Kumari, N. Sharma, S.V. Sahi, Advances in cancer therapeutics: conventional thermal therapy to nanotechnology-based photothermal therapy, Pharmaceutics 13 (2021) 1174, https://doi.org/10.3390/pharmaceutics13081174.

[3] S.H. Yun, S.J.J. Kwok, Light in diagnosis, therapy and surgery, Nat. Biomed. Eng. 1 (2017) 0008, https://doi.org/10.1038/s41551-016-0008.

[4] C.L. West Connor, L., A.C.V. Doughty, K. Liu, W.R. Chen, Monitoring tissue temperature during photothermal therapy for cancer, J. Bio-X. Res 2 (2019) 159–168, https://doi.org/10.1097/jbr. 0000000000000050.

[5] A.D. Reid, M.R. Gertner, M.D. Sherar, Temperature measurement artefacts of thermocouples and fluoroptic probes during laser irradiation at 810 nm, Phys. Med. Biol. 46 (2001) 149–157, https://doi.org/10.1088/0031-9155/46/6/403.

[6] S. Ambastha, S. Pant, S. Umesh, V. Vazhayil, S. Asokan, Feasibility study on thermography of embedded tumor using fiber bragg grating thermal sensor, IEEE Sens. J. 20 (2020) 2452–2459, https://doi.org/10.1109/JSEN.2019.2950973.

[7] S.R.H. Davidson, I.A. Vitkin, M.D. Sherar, W.M. Whelan, Characterization of measurement artefacts in fluoroptic temperature sensors: Implications for laser thermal therapy at 810 nm, Laser Surg. Med. 36 (2005) 297–306, https://doi.org/ 10.1002/lsm.20155.

[8] N.W. Lutz, M. Bernard, Contactless thermometry by MRI and MRS: advanced methods for thermotherapy and biomaterials, iScience 23 (2020) 101561 https:// doi.org/10.1016/j.isci. 2020.101561.

[9] T.J. Vogl, R. Straub, S. Zangos, M.G. Mack, K. Eichle, MR-guided laser-induced thermotherapy (LITT) of liver tumours: experimental and clinical data, Int. J. Hyperth. 20 (2004) 713–724, https://doi.org/10.1080/02656730400007212.

[10] P.P. Xu, H.H. Wu, D.D. Wang, G.Z. Zhao, F.F. Li, B.S. Qiu, Z. Guo, Q.W. Chen, Ultra-small Albumin Templated Gd/Ru composite nanodots for in vivo dual modal MR/ Thermal imaging guided photothermal therapy, Adv. Healthc. Mater. 7 (2018) 1800322, https://doi.org/10.100 2/adhm.201800322.

[11] S.H. Wang, C.W. Wei, S.H. Jee, P.C. Li, Quantitative thermal imaging for plasmonic photothermal therapy, J. Med. Biol. Eng. 31 (2011) 387–393, https://doi.org/ 10.5405/jmbe.810.

[12] U. Techavipoo, T. Varghese, Q. Chen, T.A. Stiles, J.A. Zagzebski, G. Frank, Temperature dependence of ultrasonic propagation speed and attenuation in excised canine liver tissue measured using transmitted and reflected pulses, J. Acoust. Soc. Am. 115 (2004) 2859–2865, https://doi.org/10.1121/1.1738453.

[13] J. Shah, S.R. Aglyamov, K. Sokolov, T.E. Milner, S.Y. Emelianov, Ultrasound imaging to monitor photothermal therapy – Feasibility study, 2008, Opt. Express 16 (2008) 3776–3785, https://doi.org/10.1364/OE.16.003776.

[14] M.A. Lewis, R.M. Staruch, R. Chopra, Thermometry and ablation monitoring with ultrasound, Int. J. Hyperthermia (2015) 163–181, https://doi.org/10.3109/ 02656736.2015.1009180.

[15] J. Shah, S. Park, S. Aglyamov, T. Larson, L. Ma, K. Sokolov, K. Johnston, T. Milner, S.Y. Emelianov, Photoacoustic imaging and temperature measurement for photothermal cancer therapy, J. Biomed. Opt. 13 (2008), 034024 https://doi.org/ 10.1117/ 1.2940362.

[16] A. Neprokin, C. Broadway, T. Myllyla, A. Bykov, I. Meglinski, Photoacoustic imaging in biomedicine and life sciences, Life. Basel. 12 (2022) 588, https://doi. org/10.3390/ life12040588.

[17] G. Huang, J. Lv, Y. He, J. Yang, L. Zeng, L. Nie, In vivo quantitative photoacoustic evaluation of the liver and kidney pathology in tyrosinemia, Photoacoustics 28 (2022), 100410, https://doi.org/10.1016/j.pacs.2022.100410.

[18] S. Wang, R. Chen, Q. Yu, W. Huang, P. Lai, J. Tang, L. Nie, Near-infrared plasmon-boosted heat/oxygen enrichment for reversing rheumatoid arthritis with metal/ semiconductor composites, ACS Appl. Mater. Interfaces 12 (41) (2020) 45796–45806, https://doi.org/10.1021/acsami.0c13261.

[19] J. Lv, Y. Xu, L. Xu, L. Nie, Quantitative functional evaluation of liver fibrosis in mice with dynamic contrast-enhanced photoacoustic imaging, Radiol. 300. 1 (2021) 89–97, https:// doi.org/ 10.1148/radiol.2021204134.

[20] M.W. Sigrist, Laser generation of acoustic waves in liquids and gases, 1986, J. Appl. Phys. 60 (1986) 83–122, https://doi.org/10.1063/1.337089.

[21] Q.W. Chen, J. Wen, H.J. Li, Y.Q. Xu, F.Y. Liu, S.G. Sun, Recent advances in different modal imaging-guided photothermal therapy, Biomaterials 106 (2016) 144–166, 2016. https:// doi.org/ 10. 10 16/ j.biomaterials.2016.08.022.

[22] Y.J. Liu, P. Bhattarai, Z.F. Dai, X.Y. Chen, Photothermal therapy and photoacoustic imaging via nanotheranostics in fighting cancer, Chem. Soc. Rev. 48 (2019) 2053–2108, https://doi.org/10.1039/c8cs00618k.

[23] V.R. Larina1, K.V. Larin1, R.O. Esenaliev, Real-time optoacoustic monitoring of temperature in tissues, J. Phys. D. 38 (2005) 2633–2639, https://doi.org/10.1088/ 0022-3727/38/15/015.

[24] S. Kim, Y.S. Chen, G.P. Luke, S.Y. Emelianov, In-vivo ultrasound and photoacoustic image- guided photothermal cancer therapy using silica-coated gold nanorods, IEEE Tran. Ultrason. Ferr. 61 (2014) 891–897, https://doi.org/10.1109/ TUFFC.2014.6805702.

[25] F. Landa, X. Deán-Ben, R. Sroka, D. Razansky, Volumetric optoacoustic temperature mapping in photothermal therapy, Sci. Rep. 7 (2007) 9695, https:// doi.org/10.1038/s41598-017-09069-5, 2017.

[26] Y. Zhou, M. Li, W. Liu, G. Sankin, J. Luo, P. Zhong, J. Yao, Thermal memory based photoacoustic imaging of temperature, Optica 6 (2019) 198–205, https://doi.org/ 10.1364/OPTICA.6.000198.

[27] H. Assi, C. Yang, E. Shaswary, M. Tam, J. Tavakkoli, Real-Time control of nanoparticle-mediated thermal therapy using photoacoustic imaging, IEEE Trans.

[28] Y. Yan, S. John, T. Shaik, B. Patel, M. Lam, Photoacoustic-guided endovenous laser ablation: Characterization and in vivo canine study, Photoacoustics 30 (2021), 100298, https://doi.org/10.1016/j.pacs.2021.100298.

[29] American National Standard for the Safe Use of Lasers, ANSIZ136.1–2014, 2014.

[30] C.G.A. Hoelen, F.F.M. de Mul, R. Pongers, A. Dekker, Three-dimensional photoacoustic imaging of blood vessels in tissue, Opt. Lett (1998) 648–650, https://doi.org/10.1364/ol.23.000648.

[31] M. Pramanik, L.V. Wang, Thermoacoustic and photoacoustic sensing of temperature, 2009, J. Biomed. Opt. 14 (2009), 054024, https://doi.org/10.1117/ 1.3247155.

[32] A.A. Oraevsky, S.K. Jacques, K.F. Tittle, Measurement of tissue optical properties by time-resolved detection of laser-induced transient stress, Appl. Opt. 36 (1997) 402–415, https://doi.org/10.1364/ao.36.000402.

[33] J.C. Bamber, C.R. Hill, Ultrasonic attenuation and propagation speed in mammalian tissues as a function of temperature, Ultrasound Med. Biol. 5 (1979) 149–157, https://doi.org/10.1016/ 0301-5629(79) 90083-8.

[34] C. Lai, D.E. Kruse, C.F. Caskey, D.N. Stephens, P.L. Sutcliffe, K.W. Ferrara, Noninvasive thermometry assisted by a dual-function ultrasound transducer for mild hyperthermia, IEEE Tran. Ultrason. Ferr. 57 (2010) 2671–2684, https://doi. org/10.1109/TUFFC.2010.1741.

[35] C.Y. Lai, D.E. Kruse, C.F. Caskey, D.N. Stephens, P.L. Sutcliffe, K.W. Ferrara, Noninvasive thermometry assisted by a dual-function ultrasound transducer for mild hyperthermia, Int. J. Hyperth. 57 (2010) 2671–2684, https://doi.org/ 10.1109/TUFFC.2010.1741.

[36] X. Men, X. Geng, Z. Zhang, H. Chen, M. Du, Z. Chen, G. Liu, C. Wu, Z. Yuan, Biomimetic semiconducting polymer dots for highly specific NIR-II fluorescence imaging of glioma, Mater. Today Bio 16 (2022), 100383, https://doi.org/10.1016/ j.mtbio.2022.100383.

[37] C.F. Wu, D.T. Chiu, Highly fluorescent semiconducting polymer dots for biology and medicine, Angew. Chem. Int. Ed. 52 (2022) 3086–3109, https://doi.org/ 10.1002/anie.201205133.

[38] X. Men, X. Fang, Z. Liu, Z. Zhang, C. Wu, H. Chen, Anisotropic assembly and fluorescence enhancement of conjugated polymer nanostructures, VIEW (2022), https://doi.org/10.1002/VIW.20220020.

[39] A. Sapareto, W.C. Dewey, Thermal dose determination in cancer-therapy, Int. J. Radiat. Oncol. Biol. Phys. 10 (1984) 787–800, https://doi.org/10.1016/0360-3016 (84)90379-1.

[40] H.M. Zhou, Z.H. Deng, Y.Q. Xia, M.Y. Fu, A new sampling method in particle filter based on Pearson correlation coefficient, Neurocomputing 216 (2016) 208–215, https://doi.org/10.1016/ j.neucom.2016.07.036.

[41] Z. Wang, A.C. Bovik, H.R. Sheikh, E.P. Simonce, Image quality assessment: from error visibility to structural similarity, IEEE Trans. Image Process 13 (2004) 600–612, https:// doi.org/10.1109/tip.2003.819861.

[42] L. Bianchi, S. Korganbayev, A. Orrico, M. De Landro, P. Saccomandi, Quasi-distributed fiber optic sensor-based control system for interstitial laser ablation of tissue: theoretical and experimental investigations, Biomed. Opt. Express 12 (2021) 2841–2858, https://doi.org/10.1364/ BOE.419541.

[43] A. Andreozzi, L. Brunese, M. Iasiello, C. Tucci, G.P. Vanoli, Modeling heat transfer in tumors: a review of thermal therapies, Ann. Biomed. Eng. 47 (2019) 676–693, https://doi.org/10.1007/ s10439-018-02177-x.

Dr. Kuan Peng received his B.S., M.S. and Ph.D. degree in Biomedical Engineering from Xidian University, Xi'an, China. In 2012, he joined the Department of Biomedical Engineering in Central South University, Changsha, China. His research interest includes the design and development of novel photo-acoustic and ultrasonic imaging systems for early stage cancer detection.
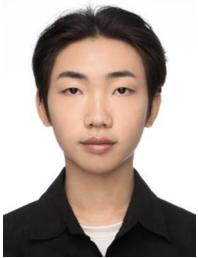
Yougjun Wang received his B.E. degree in biomedical engineering from Central South University in Changsha, China in 2020. Now he is working to pursue his master's degree in biomedical Engineering in Central South University.

Lingfeng Li received his B.E. degree in biomedical engineering from Central South University in Changsha, China in 2022. Now he is working to pursue his master's degree in biomedical Engineering in Central South University.
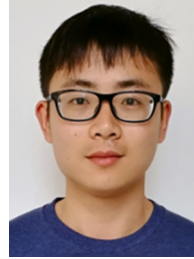
Dr. Haobin Chen obtained a B.S. in Microelectronics and a Ph. D. in Physical Electronics from the Jilin University at Changchun in 2013 and 2018. After completing postdoctoral research in Professor Daniel T. Chiu's laboratory at the University of Washington, Seattle, he started in the Spring of 2022 at the Central South University. He is the author of more than 40 publications and is the inventor on 5 issued patents. His research field of interest is activatable probes and nano-materials for ultra-sensitive bioanalytical measurements and bio-optical applications.

Jiaxi Zhang received his B.E. degree in biomedical engineering from Central South University in Changsha, China in 2022. Now he is working to pursue his master's degree in biomedical Engineering in Central South University.

Dr. Jiaying Xiao received her B.E. degree in Computer Science Engineering (2003), and her M.E. (2006) and Ph.D. (2010) degree in Biomedical Engineering in Central South University. From 2008–2010, she was a visiting scholar to the Department of Biomedical Engineering in the University of Florida. She worked in Central South University since 2007, and now is an associated professor in the School of Basic Medical Science in Central South University. Her research interest includes the early detection of cancer with photoacoustic imaging, and the reconstruction algorithm development in photoacoustic and ultrasound imaging.